Journal of Zhejiang University-SCIENCE A (Applied Physics & Engineering)
ISSN 1673-565X (Print); ISSN 1862-1775 (Online)
www.jzus.zju.edu.cn; www.springerlink.com
E-mail: jzus@zju.edu.cn

Mode transition process in a typical strut-based scramjet combustor based on a parametric study*

Lei LIAO, Li YAN, Wei HUANG†‡, Lang-quan LI

Science and Technology on Scramjet Laboratory, National University of Defense Technology, Changsha 410073, China

†E-mail: gladrain2001@163.com

Received Nov. 17, 2017; Revision accepted Mar. 7, 2018; Crosschecked May 9, 2018

Abstract: The combustion performance of hydrogen fuel in a scramjet combustor has been a popular focus for scholars all over the world. In this study, the influence of the jet-to-crossflow pressure ratio on combustion performance in a scramjet combustor was investigated numerically, and the influence of a wall-mounted cavity was evaluated. The simulations were conducted using the Reynolds-averaged Navier-Stokes (RANS) equations coupled with the renormalization group (RNG) k-ε turbulence model and the single-step chemical reaction mechanism. This numerical approach was validated by comparing predicted results with published experimental shadowgraphs and velocity and temperature measurements. When the pressure of the wall-injector increases, the performance of the combustor decreases. At the same inflow condition, this may lead to a scram-to-ram mode transition. The cavity adopted in this study would prevent pre-combustion shock waves from pushing out of the isolator and help to stabilize the flow field, but it would decrease the mixing and combustion efficiencies.

Key words: Scramjet; Mode transition; Strut; Cavity; Combustion performance
https://doi.org/10.1631/jzus.A1700617 **CLC number:** V22

1 Introduction

The dual-mode scramjet engine is the most promising propulsion system for hypersonic missions (Curran, 2001). Scramjet or ramjet engines are able to work at high temperatures because of their simple structure. Also, these engines are much lighter when providing the same thrust force as a turbine engine, and therefore they consume less fuel. Therefore, these engines should be able to work at much higher temperatures, and be lighter at the same thrust level. Hydrogen may be the most suitable fuel for these engines because of its low ignition delay and better flame stability (Choudhuri and Gollahalli, 2000; Qin et al., 2010; Cao et al., 2014). Mixing and combustion efficiency are still key issues for scramjet engines, because the fuel can stay in the combustor for only an extremely short time, namely, less than a millisecond. This issue has attracted increasing attention from scholars all over the world.

Many techniques have been proposed to improve the mixing and combustion efficiency while reducing the drag or energy loss. These techniques include different injection schemes (Turner and Smart, 2010; Kim et al., 2011; Huang et al., 2012b; Tian et al., 2015; Ogawa, 2016; Zhang et al., 2016), struts (Huang et al., 2011c; Huang, 2015; Choubey and Pandey, 2016), cavities (Micka and Driscoll, 2009; Huang et al., 2011a, 2012a, 2012d, 2016c), cantilevered ramp injectors (Huang et al., 2013, 2015), and their combinations (Fureby et al., 2015; Huang and Yan, 2016). Among these injection techniques, normal or transverse injection schemes have been the

‡ Corresponding author
* Project supported by the Fund for Owner of Outstanding Doctoral Dissertation from the Ministry of Education of China (No. 201460) and the National Natural Science Foundation of China (No. 11502291)
ORCID: Wei HUANG, https://orcid.org/0000-0001-9805-985X

subject of many recent studies (Huang and Yan, 2013; Huang, 2016). Normal or transverse injection can slow down the supersonic airstream and create separate regions in the combustor. This should help to stabilize the flame (Fureby et al., 2015).

Tian et al. (2015) investigated the combustion performance of different injection schemes computationally and experimentally (by changing the locations of wall-injectors) at different equivalence ratios. Combustion performance was judged mainly by combustion efficiency, which may offer a reference for injection schemes in different combustion modes. However, the direct influence of the jet-to-crossflow pressure ratio was unclear. Huang et al. (2014a) analyzed the influence of the jet-to-crossflow pressure ratio. They found that when injecting the hydrogen fuel from both the top and bottom walls, the separation shock wave was pushed forward to the entrance of the combustor, and the inlet unstart phenomenon could be induced. With an increasing jet-to-crossflow pressure ratio, the mixing efficiency decreased. These results confirmed the conclusions from their previous study (Huang et al., 2012b). However, combustion efficiency was not analyzed.

The combination of wall-injection and a strut or cavity has also been investigated by many scholars. The strut and injectors on a strut can produce a recirculation region in the combustion area, which would stabilize the flame effectively. However, this method may cause a great pressure loss when the inflow enters at a high Mach number (Gang et al., 2011). A cavity draws fuel into it, creating a vortex nearby. Thus, it can act as a stable flame holder, and would cause much less pressure loss than a strut (Gruber, 2004). Micka and Driscoll (2009) observed two different combustion stabilization modes when placing a wall-injector in front of a cavity, namely cavity stabilized combustion and jet-wake stabilized combustion. The difference between these modes is caused mainly by different equivalence ratios. Huang et al. (2016b) investigated a typical strut-based scramjet combustor numerically, with a wall-injector set at a distance of 15 mm behind the strut. Their results showed that an increase in the jet-to-crossflow pressure ratio expanded the subsonic area, but the variation in combustion efficiency in different cases was not clear.

For the same injector configuration, the jet-to-crossflow pressure ratio determines the equivalence ratio and affects the combustion mode in the combustor. Therefore, it is necessary to investigate the combustion performance of cases with different jet-to-crossflow pressure ratios. The results may provide a reference for the design of dual-mode scramjet combustors.

In this paper, the influence of the jet-to-crossflow pressure ratio on combustion performance was investigated numerically, with the inflow entering at four different Mach numbers, namely 1.7, 1.9, 2.1, and 2.3. The jet-to-crossflow pressure ratio of the wall-injector varied from 0 to 3.43, while that of the strut-injector was fixed at 3.43 to ensure that the equivalence ratio would be in a reasonable range, namely from about 0.2 to 0.7. The influence of a cavity was also evaluated.

2 Physical model and numerical method

2.1 Physical model

The physical model utilized in the current study was based on a typical strut-based dual-mode scramjet combustor. The German Aerospace Center tested a similar model (Oevermann, 2000). Huang et al. (2016b) conducted a numerical study on this model as well. Fig. 1 shows a schematic diagram of this model, and its detailed information can refer to Yan et al. (2018). Air entered the isolator at four different Mach numbers, namely Ma=1.7, 1.9, 2.1, and 2.3. Details of the parameters are shown in Table 1. The fuel was injected into the combustor horizontally at the local sonic velocity, and its total temperature was fixed at 1200 K. The jet-to-crossflow pressure ratio of the jet was fixed at 3.43 on the strut, and varied from about

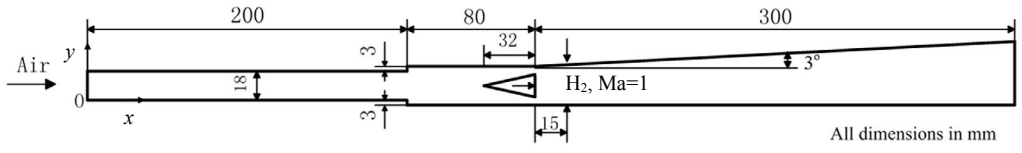

Fig. 1 Schematic diagram of the strut-based dual-mode scramjet combustor

1.7 to 3.43 on each wall. The composition of the air was set at 23.2% O_2, 0.032% H_2O, and 73.6% N_2, and the fuel was pure hydrogen (H_2).

Table 1 Details of the parameters of the air for different Mach numbers

Ma	Total temperature (K)	Static pressure (atm)	Total pressure (atm)
1.7	900	1.46	7.2
1.9	1300	2.21	14.8
2.1	1810	3.20	29.3
2.3	2400	3.90	48.7

1 atm=101.325 kPa

2.2 Numerical method

Numerical simulations were conducted using Fluent 6.3.26 (Fluent, 2006). Two-dimensional compressible Reynolds-averaged Navier-Stokes (RANS) equations were adopted in this study, and the advection upstream splitting method (AUSM) and the implicit second-order upwind scheme were employed for spatial discretization. A density-based implicit solver was utilized. The turbulence model chosen was a two equation renormalization group (RNG k-ε) model (Huang et al., 2011b). According to Huang et al. (2011c), this model proved to be more accurate than the shear stress transport (SST) k-ω model in simulating the flow field of transverse slot cases when the jet-to-crossflow pressure ratio was relatively low (lower than 10). A comparison between the predicted results obtained by the RNG k-ε and SST k-ω models is shown in Section 3.

The governing equations were as follows (Huang et al., 2012c; Kummitha et al., 2018):

$$\frac{\partial}{\partial t}(\rho Y_i)+\frac{\partial}{\partial x_j}(\rho u_j Y_i)=-\frac{\partial}{\partial x_i}(\rho \breve{u}_i Y_i)+\omega_i, \tag{1}$$

$$\frac{\partial \rho}{\partial t}+\frac{\partial}{\partial x_i}(\rho u_i)=0, \tag{2}$$

$$\frac{\partial(\rho u_i)}{\partial t}+\frac{\partial}{\partial x_i}(\rho u_i u_j)=-\frac{\partial P}{\partial x_i}+\frac{\partial \boldsymbol{\tau}_{ij}}{\partial x_i}, \tag{3}$$

$$\frac{\partial(\rho e_\mathrm{t})}{\partial t}+\frac{\partial}{\partial x_i}(\rho h_\mathrm{t} u_j)=\frac{\partial}{\partial x_i}(\boldsymbol{\tau}_{ij}u_i-\boldsymbol{q}_i), \tag{4}$$

where Y_i is the mass fraction of chemical species, ρ is the gas density, and u_i and u_j are the velocity components in the x_i and x_j directions, respectively. P is the pressure, and h_t is the total enthalpy per unit volume. The heat flux vector $\boldsymbol{q}_i$ due to conduction and convection is given as

$$\boldsymbol{q}_i=-\lambda\frac{\partial T}{\partial x_j}+\rho\sum_{k=1}h_k Y_k u_{\breve{j},k}, \tag{5}$$

where λ is the thermal conductivity, and T is the static temperature. The diffusion velocities $u_{\breve{j},k}$ were calculated using Fick's law, which is given as

$$Y_k u_{\breve{j},k}=-D_{k,\mathrm{m}}\frac{\partial}{\partial x_j}Y_k. \tag{6}$$

The stress tensor $\boldsymbol{\tau}_{ij}$ was calculated using the Boussinesq hypothesis, which relates the Reynolds stresses to the mean strain tensor and is defined as

$$\boldsymbol{\tau}_{ij}=(\mu+\mu_\mathrm{t})\left[\frac{\partial u_i}{\partial x_j}+\frac{\partial u_j}{\partial x_i}-\frac{2}{3}\delta_{ij}\frac{\partial u_k}{\partial x_k}\right]-\frac{2}{3}\rho k\delta_{ij}, \tag{7}$$

where μ and μ_t are the molecular and turbulent viscosity coefficients, respectively. ω_i is the chemical source term of species i, and is calculated directly using temperature, density, and species mass fractions:

$$\omega_i=\omega_i(\rho, Y_1, Y_2, \cdots, T). \tag{8}$$

e_t is the total energy per unit volume, and

$$e_\mathrm{t}=\sum_{i=1}Y_i h_i+\frac{1}{2}(u^2+v^2+w^2)-\frac{P}{\rho}, \tag{9}$$

where u, v, and w are the Cartesian velocity components in x, y, and z directions, respectively. The state equation of gas is

$$P=\rho RT\sum_{i=1}\frac{Y_i}{W_i}, \tag{10}$$

where R is the universal constant of gas. W_i, $D_{k,\mathrm{m}}$, and h_i are the molecular weight, mass diffusion coefficient, and absolute enthalpy per unit mass of species i, respectively.

The transport equations for k and ε can refer to Yan et al. (2018).

To reduce the computational cost, the single step chemical reaction of hydrogen combustion was employed in this study, and this is the same as that conduct by Yan et al. (2018).

The laminar finite rate model was adopted here to simulate intense turbulent combustion, and it can refer to Yan et al. (2018).

The boundary conditions were set to the pressure-inlet for both the isolator entrance and the fuel jets, and the pressure-outlet for the combustion outlet. All the walls were fixed with no-slip condition. The Courante-Friedrichs-Lewy (CFL) number was taken as 0.5 at first, and as 2 or 5 to accelerate the convergence when the computations became more stable. All the gases were assumed to be ideal gases, and their viscosity and thermal conductivities were computed using the mass-weighted-mixing-law, while the specific heat (C_p) was computed using the mixing-law.

The grids were generated using Gambit (Fluent, 2006), and the scale of the grid was about 100 000 (Section 3). The grids were refined near the walls, steps, strut, and fuel jet, so that the boundary layer or shock-wave at important locations could be predicted accurately. The height of the first cell near the walls was 0.01 m, which ensured that the value of y^+ (a non-dimensional parameter defined by Huang et al. (2016a)) was proper for all the flow fields, namely its maximum value was less than 25.0. A close-up view of the grid around the strut and steps is shown in Fig. 2.

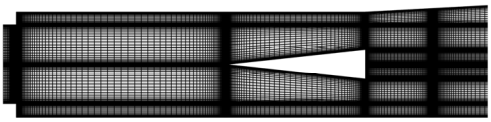

Fig. 2 A close-up view of the grid

3 Code validation

A typical dual-mode scramjet combustor was used to provide data for evaluation of the numerical method. The combustor (Fig. 3) was tested at the German Aerospace Center (Oevermann, 2000), and its detailed information can refer to Yan et al. (2018). The details of the parameters of this experiment are listed in Table 2.

According to the recent literature, both the two equation renormalization group (RNG k-ε) model and the two equation shear stress transport (SST k-ω) model are commonly used for these cases. The influence of turbulence on the chemical kinetics can be simulated following the approaches developed using the Gaussian quadrature technique (Smirnov et al., 2010; Smirnov and Nikitin, 2014). The RNG k-ε model was selected for its robustness and its ability to fit the initial iteration (Guerra et al., 1991), while the SST k-ω model is better suited for prediction of mixing layers and jet flows (Huang et al., 2012c). The figures below compare the results computed by the two turbulence models based on the same settings, such as mesh scales, reaction model, and boundary conditions.

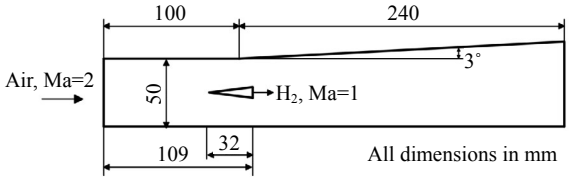

Fig. 3 A schematic of a typical dual-mode combustor

Table 2 Details of the parameters of the experiment

Parameter	Value	
	Air	Hydrogen fuel
Ma	2.0	1.0
Static temperature (K)	340	250
Static pressure (atm)	1.0	1.0
Y_{O_2}	0.232	0
Y_{N_2}	0.736	0
Y_{H_2O}	0.032	0
Y_{H_2}	0	1

Fig. 4 shows a comparison of density contours obtained using different turbulence models without combustion, and an experimental shadowgraph. We can see that the density contours obtained by the two turbulence models were nearly the same. When compared with Fig. 4c, the flow fields obtained by numerical simulation were clearly very similar to those from experimentation. The first shock wave is formed at the tip of strut, and then reflected on the walls. While the first expansion wave is formed at the tail of the strut, it is also reflected on the walls. There

is a complicated interaction phenomenon between shock waves and expansion waves. However, there are some differences between the computational fluid dynamics (CFD) simulation and the experiment as well. For example, in the experimental shadowgraph (Fig. 4c) the fuel-air mixing layer is rapidly weakened downstream of the first intersection of the reflected shock waves, and nearly disappears at the second intersection point. In the two density contours obtained by numerical simulation, that mixing layer remains obvious, even at the second intersection point.

Fig. 5 shows a comparison of density contours obtained by the different turbulence models with combustion, and an experimental shadowgraph. The two density contours obtained by CFD are very similar to each other. Comparison with Fig. 5c shows that the reaction zone predicted by numerical simulation is broader than that obtained by the experiment. Also, the decay rate of waves is greater, while the flow fields are similar. Shock waves formed at the tip and expansion waves formed at the tail of the strut are reflected between the wall and the fuel-air mixing layer. The reaction zone slowly broadens reaching its maximum width when the expansion waves are reflected from the reaction zone boundary. To sum up, both turbulence models can predict the combustion flow field structures suitably.

Fig. 6a shows a comparison of wall static pressures obtained by the two turbulence models and by experiment. The pressure distributions obtained by both models fit well with the experimental data at most points, but there is some deviation in the prediction of peak values at x=120 mm and 170 mm. This may be caused by the assumption of a 2D model, and these results should be validated by a 3D simulation in the near future. The stochastic error accumulation is proportional to the number of time steps and depends on the accuracy of the scheme and its approximation error (Smirnov et al., 2015), but this is

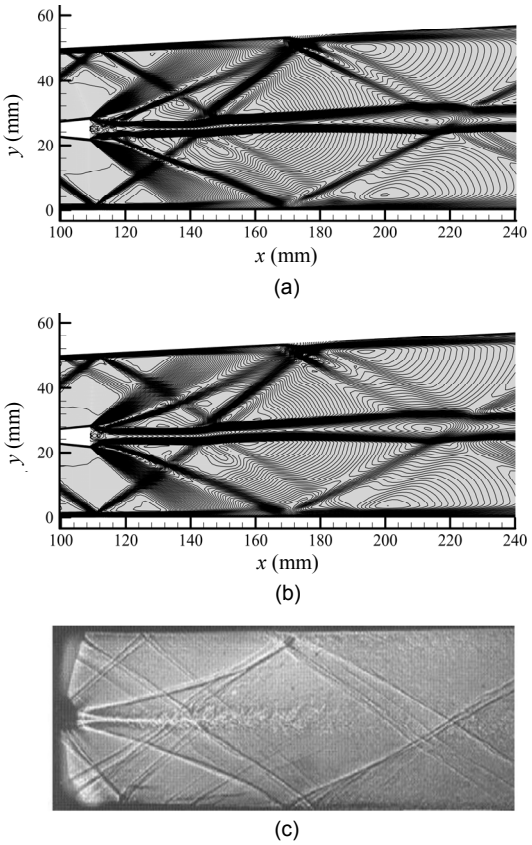

Fig. 4 Flow field comparison without combustion
(a) Density contour obtained by RNG k-ε; (b) Density contour obtained by SST k-ω; (c) Experimental shadowgraph

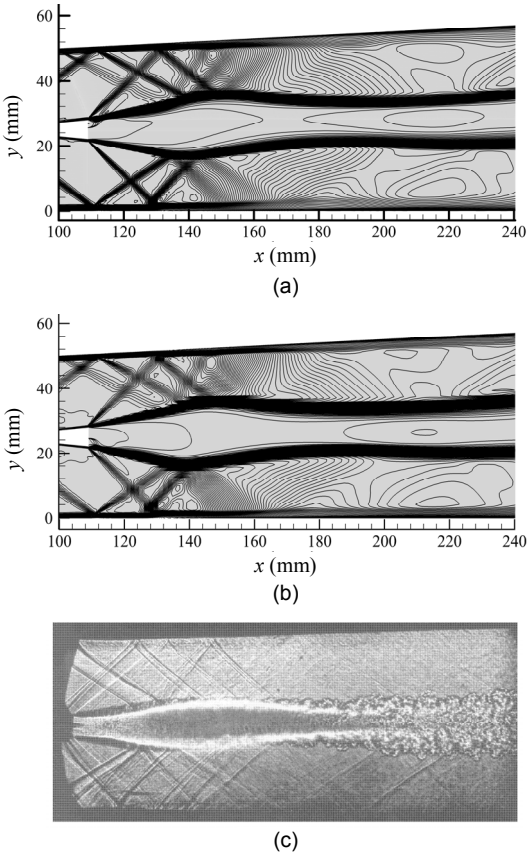

Fig. 5 Flow field comparison with combustion
(a) Density contour obtained by RNG k-ε; (b) Density contour obtained by SST k-ω; (c) Experimental shadowgraph

beyond the scope of this paper. Fig. 6b shows a comparison of horizontal velocity distributions along the middle line (y=25 mm). The predicted results obtained by the two models differ from the experimental data at the maximum and minimum values, but the variable trends are similar. At this point, the RNG k-ε model has a slight advantage over the SST k-ω model. Both models can predict most features of the flow field, but the RNG k-ε model would be slightly better than the SST k-ω model in this case.

Fig. 7 shows the horizontal velocity profiles at three different streamwise cross-sections (x), namely

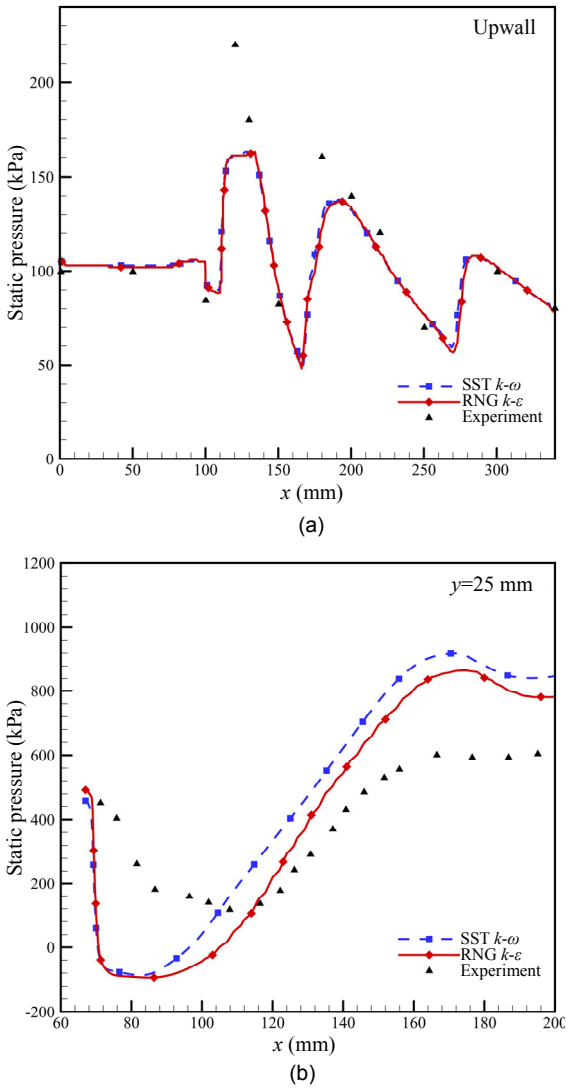

Fig. 6 Comparison of wall static pressures obtained by the two turbulence models and by experiment (a) and horizontal velocity distributions along the middle line (y=25 mm) (b)

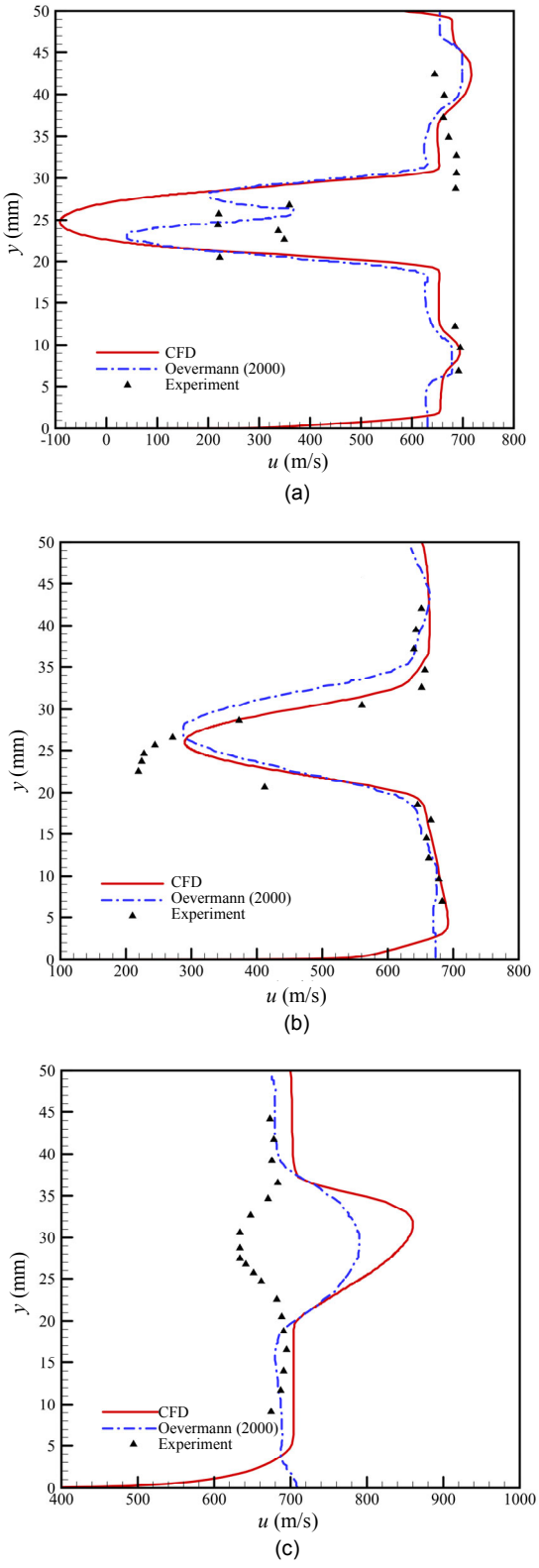

Fig. 7 Horizontal velocity profiles at three different streamwise cross-sections: (a) x=78 mm; (b) x=125 mm; (c) x=207 mm

(a) x=78 mm, (b) x=125 mm, and (c) x=207 mm, compared with the results obtained by Oevermann (2000). In Fig. 7a, the peak value at y=25 mm obtained by CFD is lower than that of the experimental data. This is because the reaction model used here would cause a higher heat release rate, and the horizontal velocity near the fuel jet would be smaller than it should be. In Fig. 7b, the profiles obtained by CFD fit well with the experimental data. In Fig. 7c, the profiles obtained by CFD are quite different from those of the experimental data in the range 20 mm< y<40 mm. This deviation may be inherent in this kind of simulation.

Fig. 8 shows the static temperature profiles at three different streamwise cross-sections, namely (a) x=78 mm, (b) x=125 mm, and (c) x=233 mm, compared with the results of Oevermann (2000). In Fig. 8a, the CFD results have only one peak value while the experimental results have two, resembling the results of the horizontal velocity profiles at x= 78 mm. In Fig. 8b, the CFD results are more similar to the experimental data compared to the results of Oevermann (2000), but the peak value is a little larger than that of the experimental data. In Fig. 8c, the static temperature obtained by CFD is higher than that of Oevermann (2000) and the experimental data at 20 mm<x<40 mm, and this might be induced by the deviation of the reaction model.

The grid independency analysis for this physical model was conducted by Yan et al. (2018), and a mesh scale over 101 400 would not greatly affect the simulation. Therefore, the mesh with 101 400 nodes was chosen to carry out the following simulation in order to save computing resource.

4 Results and discussion

4.1 Strut-based combustor

The combustor was numerically simulated under four different inflow conditions, namely Ma=1.7, 1.9, 2.1, and 2.3. There were five different injection schemes (cases a, b, c, d, and e) for each inflow condition. Table 3 shows the value of wall-injection pressure $P_{j\text{-}w}$ for different inflow conditions. For each inflow condition, the pressure of strut-injection was fixed at 3.43 times the inflow pressure.

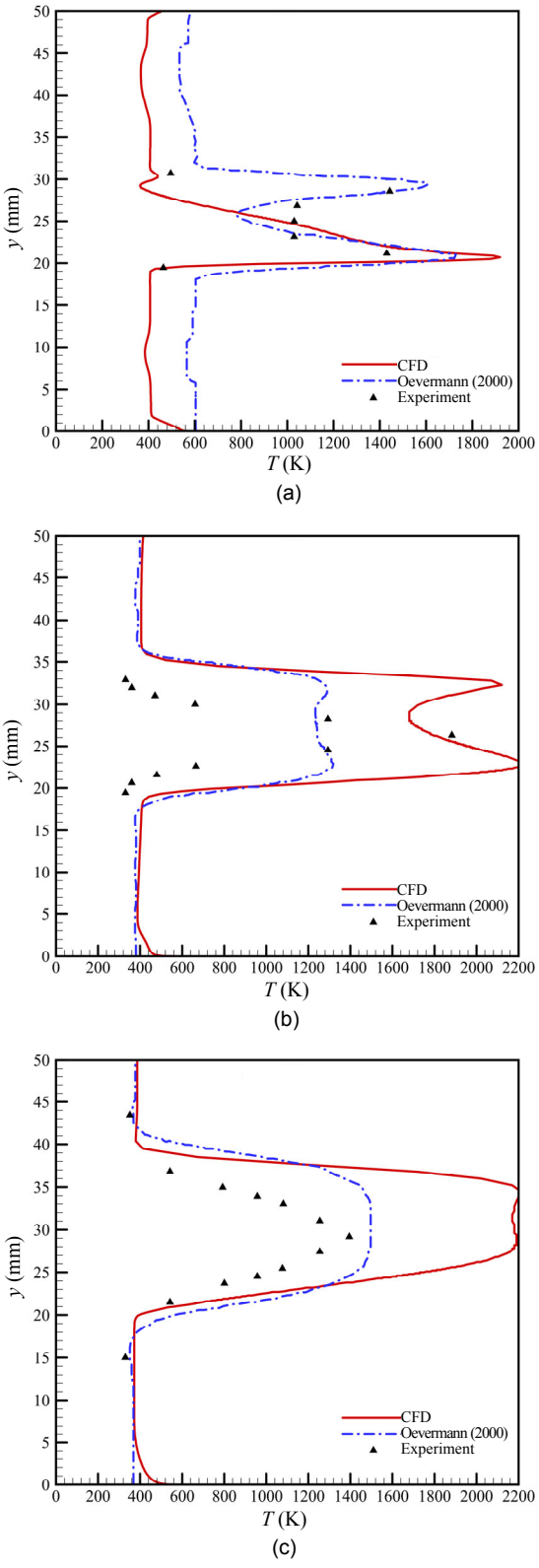

Fig. 8 Static temperature profiles at three different streamwise cross-sections: (a) x=78 mm; (b) x=125 mm; (c) x=233 mm

4.1.1 Inlet Mach number of 1.7

Fig. 9 shows a comparison of the Mach number contours and wave structures with different wall-injection pressures $P_{j\text{-}w}$ when the air enters at Ma=1.7. For these five cases, the strut-injection pressure $P_{j\text{-}s}$ was fixed at 5.0 atm, which was 3.43 times the static pressure of the main flow. Clearly, when $P_{j\text{-}w}$ increases from 0 to 4.0 atm, the pre-combustion shock waves move towards the entrance of isolator. When $P_{j\text{-}w}\geq 3.5$ atm, the pre-combustion shock waves would be pushed out of the isolator, and this would have a great effect on the inlet performance. The flow field downstream of the strut also clearly differs.

Table 3 Wall-injection pressure for different cases

Case	Wall-injection pressure (atm)			
	Ma=1.7	Ma=1.9	Ma=2.1	Ma=2.3
a	0	0	0	0
b	2.5	4.0	6.0	7.0
c	3.0	5.0	7.5	9.0
d	3.5	6.0	9.0	11.0
e	4.0	7.58	10.99	13.36

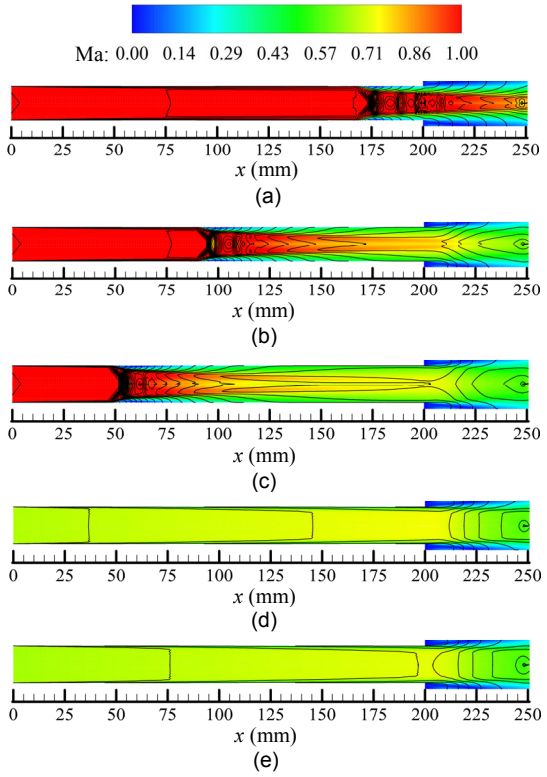

Fig. 9 Comparison of the Mach number contours and wave structures at different wall-injection pressures: (a) $P_{j\text{-}w}$=0; (b) $P_{j\text{-}w}$=2.5 atm; (c) $P_{j\text{-}w}$=3.0 atm; (d) $P_{j\text{-}w}$=3.5 atm; (e) $P_{j\text{-}w}$=4.0 atm

Fig. 10 shows a comparison of combustion performance for different wall-injection pressures when the main flow enters at Ma=1.7. Performance parameters include mixing efficiency η_m, combustion effciency η_c, mass-weighted average Mach number, and total pressure recovery σ_i. Higher mixing and combustion efficiency means better fuel economy, while a higher average Mach number and total pressure recovery means a lower energy loss. The definitions of mixing efficiency η_m and combustion effciency η_c are as follows (Segal, 2009):

$$\eta_m=\frac{\dot{m}_{fuel,mixed}}{\dot{m}_{fuel,total}}=\frac{\int \alpha_{react}\rho u\mathrm{d}A}{\int \alpha\rho u\mathrm{d}A}. \tag{11}$$

Herein,

$$\alpha_{react}=\begin{cases}\alpha, & \alpha\leq\alpha_{stoic},\\ \alpha(1-\alpha)/(1-\alpha_{stoic}), & \alpha>\alpha_{stoic},\end{cases} \tag{12}$$

$$\eta_c=1-\frac{\bar{\alpha}}{\alpha_0}=1-\frac{\bar{\alpha}}{\dot{m}_{fuel,total}/\dot{m}_{total}}, \tag{13}$$

where α is the located mass fraction of fuel, α_{react} is the fraction of fuel that has been well mixed and can react, and α_{stoic} is the stoichiometric mass fraction (for H_2, this value should be 0.0293) (Huang et al., 2016b). $\bar{\alpha}$ is the mass-weighted average mass fraction of fuel at one section, and α_0 is the initial fraction of fuel. $\dot{m}_{fuel,total}$ is the total injectant flow rate, and $\dot{m}_{total}$ is the total flow rate. As the wall-injection pressure $P_{j\text{-}w}$ increases, the mixing efficiency η_m takes longer to reach 1.0 (Fig. 10a). When there is no wall-injection, η_m is higher at first, then soon becomes lower than that of the case with $P_{j\text{-}w}$=2.5 atm, but remains higher than those of other cases. This indicates that proper wall-injection would improve the degree of turbulence of the flow field. As the wall-injection pressure $P_{j\text{-}w}$ increases, the combustion efficiency η_c decreases monotonically (Fig. 10b). For all cases with wall-injection, the growth rates of η_c are high at first, but then decline, indicating that most of the chemical reaction process takes place in the first half of the combustor. When there is wall-injection, the subsonic region is much larger (Fig. 10c), and for all cases with

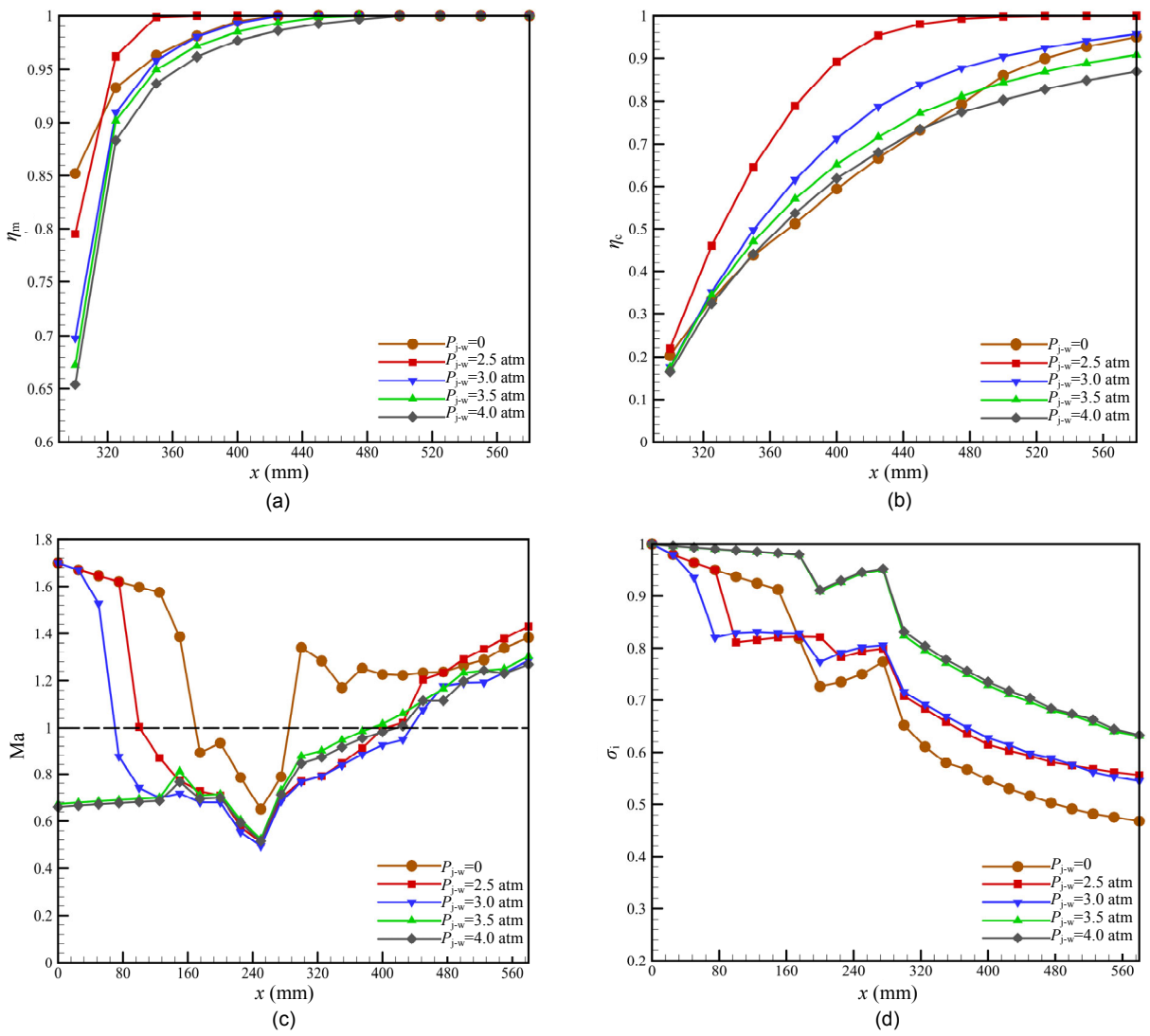

Fig. 10 Comparison of combustion performance at different wall-injection pressures when the main flow enters at Ma=1.7: (a) mixing efficiency; (b) combustion efficiency; (c) mass-weighted Mach number; (d) total pressure recovery

wall-injection, the combustor works in ramjet mode. This is judged by the average Mach number at the interval 300 mm<x<400 mm. When the combustor works normally (pre-combustion still in isolator, namely $P_{j\text{-}w}$=2.5 or 3.5 atm), the pressure recoveries are similar, and obviously larger than in the case with only strut injection (Fig. 10d).

4.1.2 Inlet Mach number of 1.9

Fig. 11 shows a comparison of the Mach number contours and wave structures with different wall-injection pressures $P_{j\text{-}w}$ when the air enters at Ma=1.9. For these five cases, the strut-injection pressure $P_{j\text{-}s}$ is fixed at 7.58 atm, which is 3.43 times the static pressure of the main flow. When the Mach number of the main flow increases to 1.9, the pre-combustion is not pushed out of the isolator, but it is still pushed away from the inlet of the combustor slightly when the wall-injection pressure increases. Apart from the variation in the flow field in front of the strut, there are no significant differences in Figs. 11b–11e.

Fig. 12 shows a comparison of the combustion performance for different wall-injection pressures when the main flow enters at Ma=1.9. In Figs. 12a and 12b, we can still see the same trend in η_m and η_c when the wall-injection pressure varies, namely they

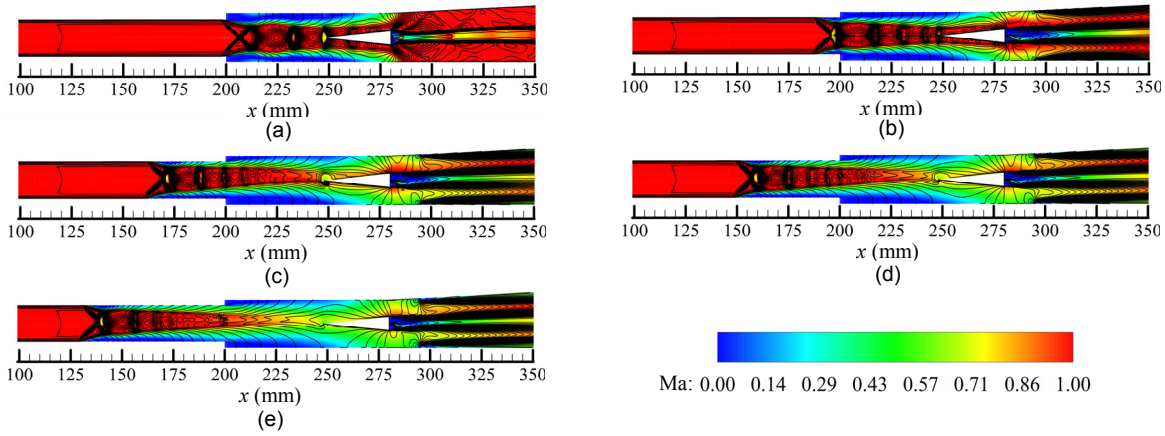

Fig. 11 Comparison of the Mach number contours and wave structures with different wall-injection pressures at Ma=1.9
(a) $P_{j\text{-}w}$=0; (b) $P_{j\text{-}w}$=4.0 atm; (c) $P_{j\text{-}w}$=5.0 atm; (d) $P_{j\text{-}w}$=6.0 atm; (e) $P_{j\text{-}w}$=7.58 atm

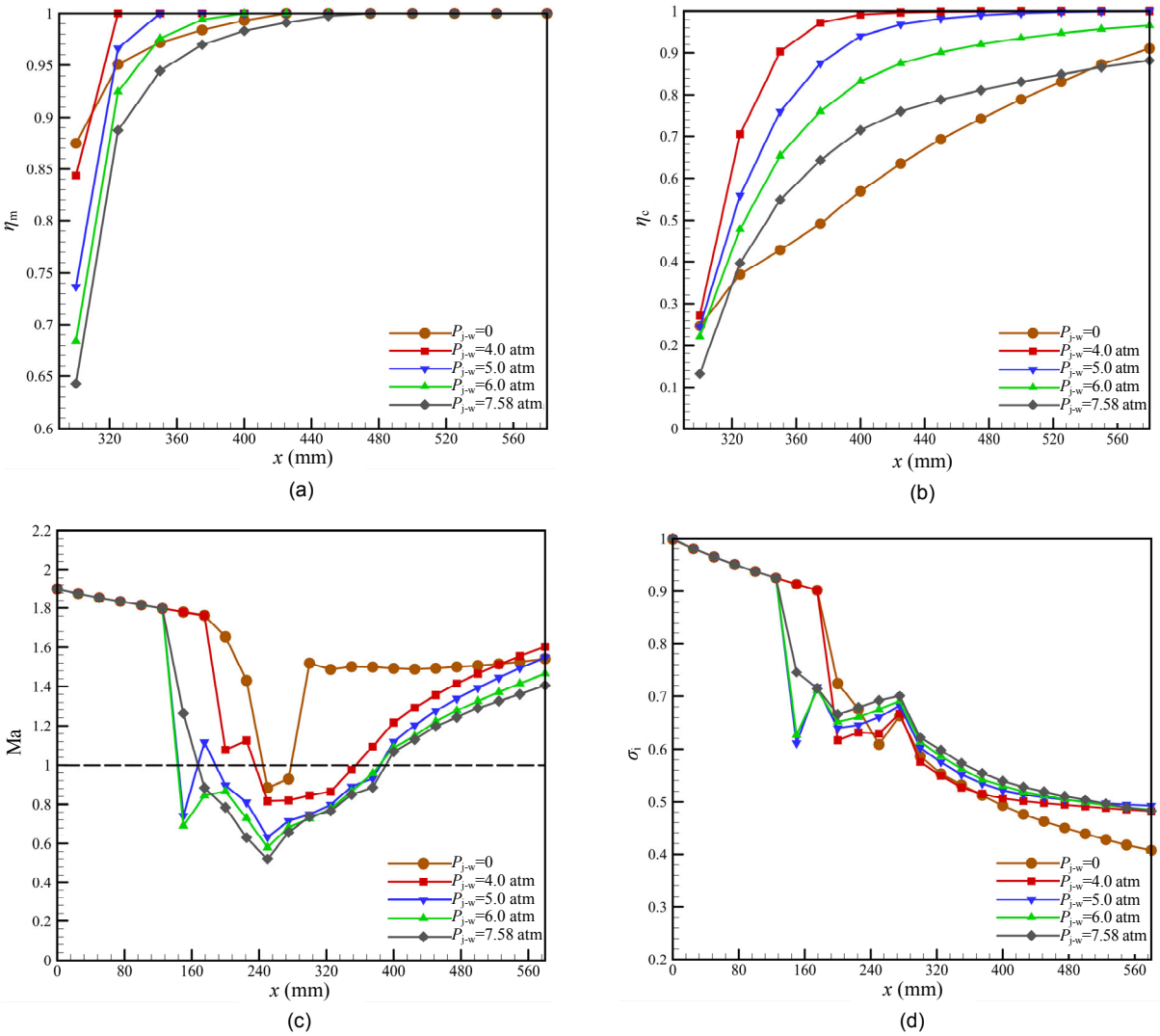

Fig. 12 Comparison of combustion performance at different wall-injection pressures when the main flow enters at Ma=1.9
(a) Mixing efficiency; (b) Combustion efficiency; (c) Mass-weighted Mach number; (d) Total pressure recovery

decrease when $P_{j\text{-}w}$ increases. However, in the case without wall-injection, performance is poor: its mixing efficiency is better only than that of $P_{j\text{-}w}$=7.58 atm and its combustion efficiency is the lowest. In Fig. 12c, there are significant differences between cases, and in the case with $P_{j\text{-}w}$=4.0 atm a mode transition is about to occur (its Mach number at 300 mm <x<400 mm is around 1.0) (Huang et al., 2014b). In the cases with $P_{j\text{-}w}$≥5.0 atm the combustor is still working in ramjet mode, and it would work in scramjet mode when there is no wall-injection. In Fig. 12d, cases with wall-injection have a similar total pressure recovery at the outlet, which is apparently higher than in the case with only strut-injection.

4.1.3 Inlet Mach number of 2.1

Fig. 13 shows a comparison of the Mach number contours and wave structures with different wall-injection pressures $P_{j\text{-}w}$ when the air enters at Ma=2.1. For these five cases, the strut injection pressure $P_{j\text{-}s}$ is fixed at 10.99 atm, which is 3.43 times the static pressure of the main flow. For all cases, the main flow enters the combustor at supersonic speed. As the wall-injection pressure $P_{j\text{-}w}$ increases, the pre-combustion shock waves generated at the entrance of the combustor gradually strengthen. As a result, the separation zones generated on the upper and lower walls gradually grow. When $P_{j\text{-}w}$=10.99 atm, there are some small subsonic regions in front of the strut.

Fig. 14 shows a comparison of combustion performance for different wall-injection pressures when the main flow enters at Ma=2.1. In Figs. 14a and 14b, the mixing and combustion efficiency decreases slightly when the wall-injection pressure decreases. In Fig. 14c, in the cases with $P_{j\text{-}w}$≥7.5 atm, the main flow decelerates to subsonic at the tip of the strut (about x=250 mm), and then accelerates to supersonic at about x=350 mm. Thus, these cases may be at the transition point of ram to scram. The average Mach number decreases as the wall-injection pressure decreases. Note that compared with the cases with air entering at lower Mach numbers, the average Mach number is the largest. In Fig. 14d, the curves obtained by different wall-injection pressures are almost the same, and a little higher than those in the case without wall-injection at about 0.5.

4.1.4 Inlet Mach number of 2.3

Fig. 15 shows a comparison of the Mach number contours and wave structures with different wall-injection pressures $P_{j\text{-}w}$ when the air enters at Ma=2.3. For these five cases, the strut-injection pressure $P_{j\text{-}s}$ is fixed at 13.36 atm, which is 3.43 times the static pressure of the main flow. The main flow does not decelerate to subsonic until it reaches the tip of the strut, and the pre-combustion shock waves have been totally swallowed. As the wall-injection pressure increases, the separation zones generated on the up and lower walls and at the tip of the strut gradually grow, and the separation zones in front of the wall injections become larger. For cases with $P_{j\text{-}w}$≤9.0 atm, the flow field is seriously asymmetric (Figs. 15a–15c).

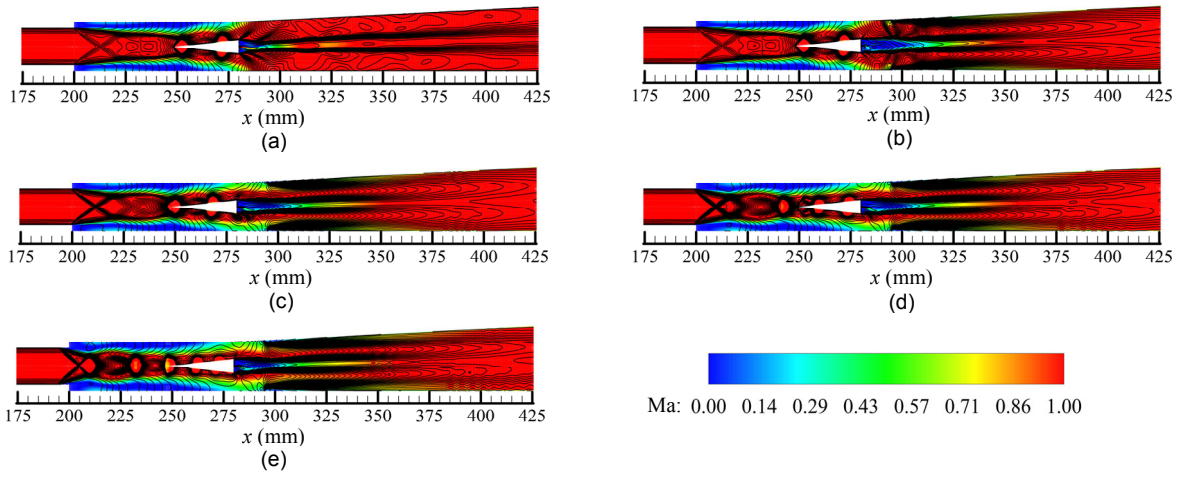

Fig. 13 Comparison of the Mach number contours and wave structures with different wall-injection pressures at Ma=2.1
(a) $P_{j\text{-}w}$=0; (b) $P_{j\text{-}w}$=6.0 atm; (c) $P_{j\text{-}w}$=7.5 atm; (d) $P_{j\text{-}w}$=9.0 atm; (e) $P_{j\text{-}w}$=10.99 atm

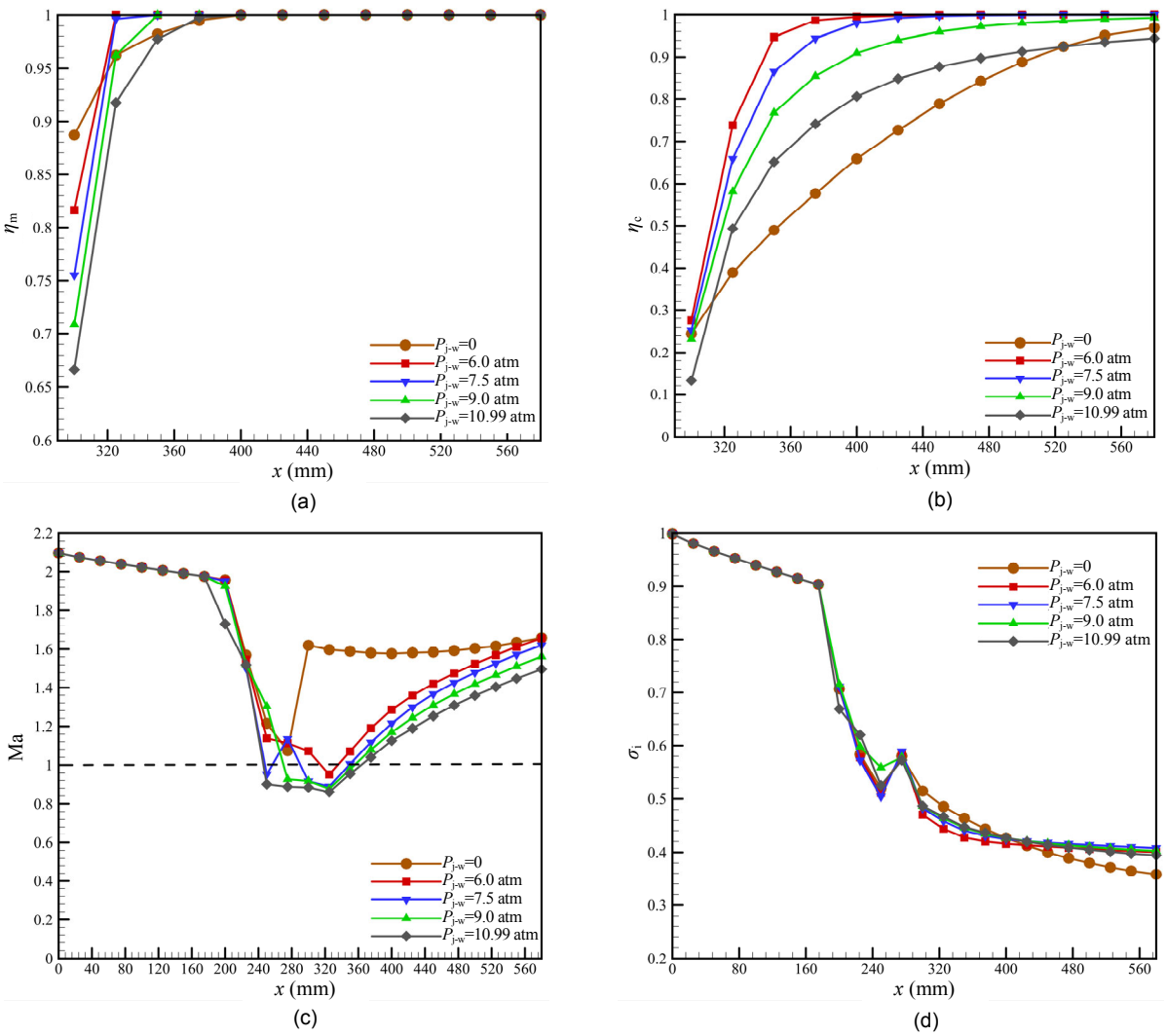

Fig. 14 Comparison of combustion performance at different wall-injection pressures when the main flow enters at Ma=2.1
(a) Mixing efficiency; (b) Combustion efficiency; (c) Mass-weighted Mach number; (d) Total pressure recovery

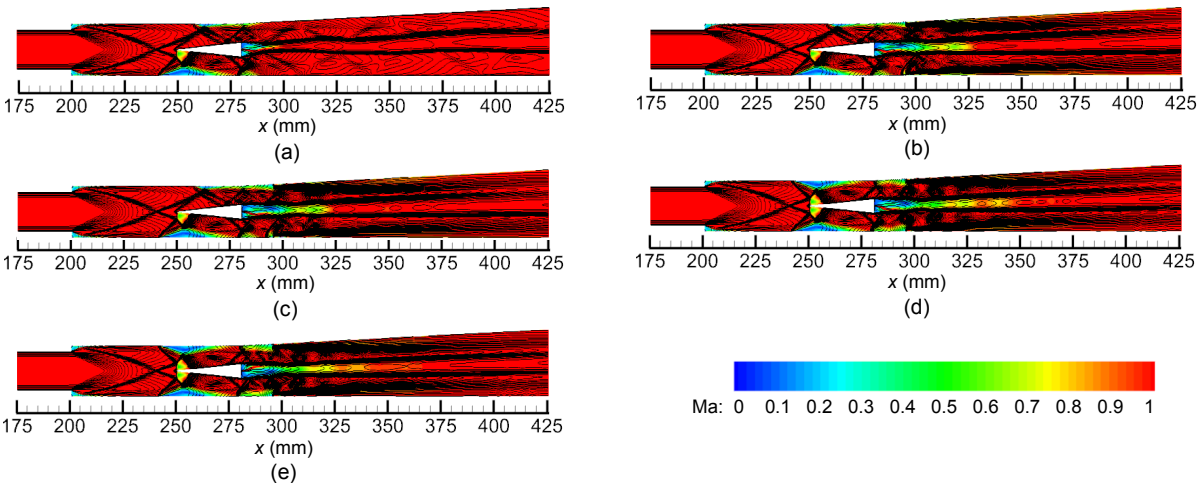

Fig. 15 Comparison of the Mach number contours and wave structures with different wall-injection pressures at Ma=2.3
(a) $P_{j\text{-}w}$=0; (b) $P_{j\text{-}w}$=7.0 atm; (c) $P_{j\text{-}w}$=9.0 atm; (d) $P_{j\text{-}w}$=11.0 atm; (e) $P_{j\text{-}w}$=13.36 atm

There is a large subsonic separation zone on the bottom wall near the tip of the strut, but only a very small one at the same location on the top wall.

Fig. 16 shows a comparison of combustion performance for different wall-injection pressures when the main flow enters at Ma=2.3. As observed above, the mixing and combustion efficiency decreases as the wall-injection pressure increases, but the combustion for the case without wall-injection is the lowest. This indicates that the fuel has insufficient time for reaction at such a Mach number in this case. The average Mach number obtained by the case with only strut-injection is much higher than that obtained by the others (Fig. 16c). This indicates that injection into a main flow of Ma=2.3 in such a way would cause a huge loss of energy. The total pressure obtained by the case with only strut-injection is higher than those obtained by the others (Fig. 16d), and this is opposite to the results observed above. This suggests that the additional heat release cannot counteract the loss of energy caused by wall-injection. Therefore, a more efficient and stable combustion organization is required for this high Mach number.

4.2 Strut-cavity combustor

The discussion above indicates that the combustor with a single strut employed here has some defects in some cases. For example, it would push the

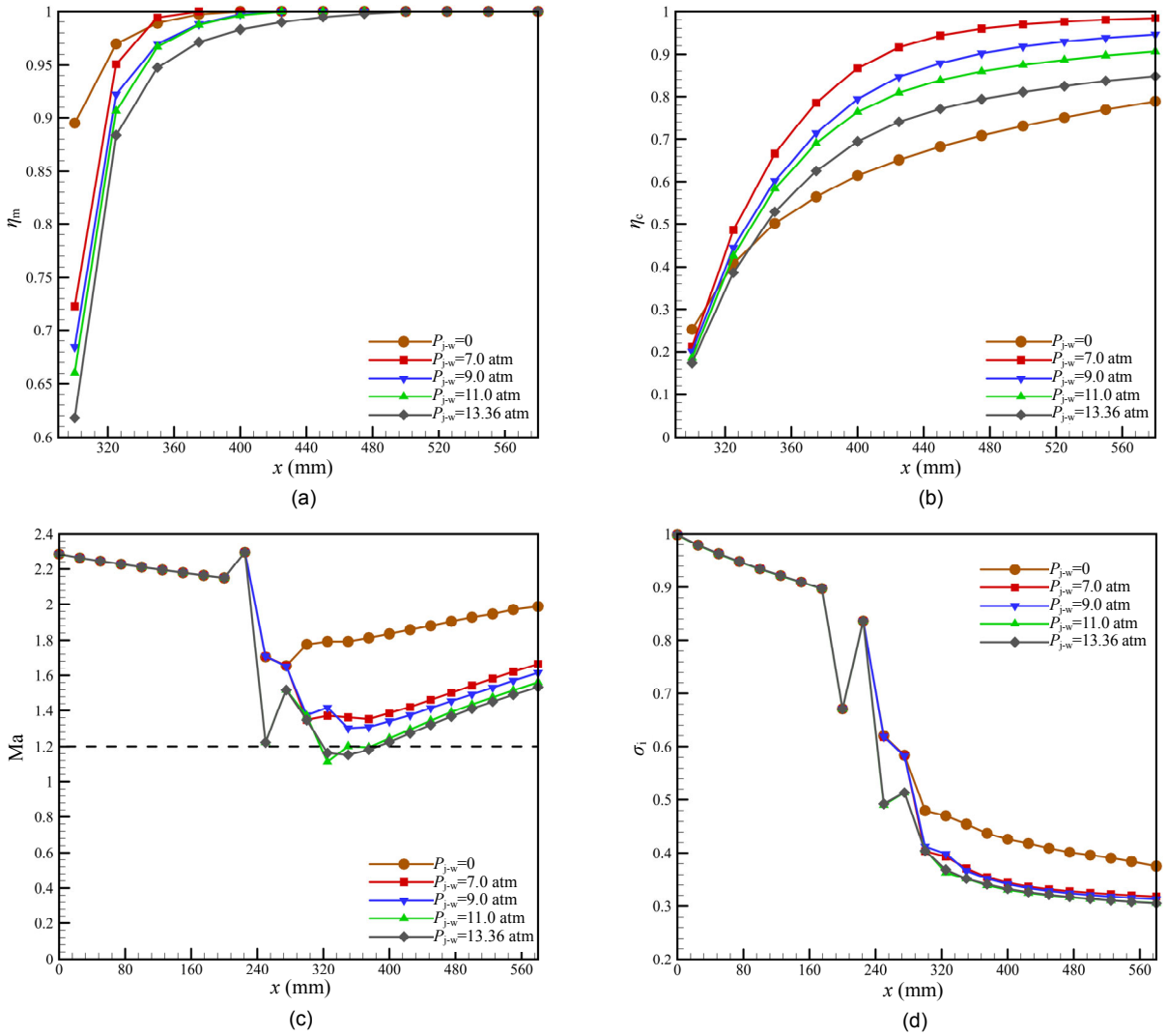

Fig. 16 Comparison of combustion performance at different wall-injection pressures when the main flow enters at Ma=2.3
(a) Mixing efficiency; (b) Combustion efficiency; (c) Mass-weighted Mach number; (d) Total pressure recovery

pre-combustion shock waves out of the isolator easily when operating in ramjet mode, and would not be stable enough or suffer too much energy loss when operating in scramjet mode.

In this section, we discuss the results when two cavities are added to this combustor (Fig. 17). The cavities are symmetrical about the centerline, and are 5 mm high and 15 mm wide. The trailing edge of the cavities is at 45°. The cavities used here are a kind of typical open cavity, and provide a large low-velocity area for the diffusion and combustion of fuel. In the following section, we describe the results of numerical simulations conducted using the same settings. The only different variable is the combustor model.

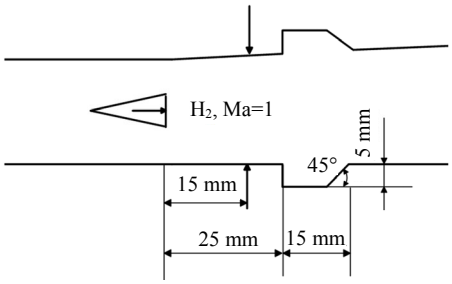

Fig. 17 Location and size of the cavities

4.2.1 Inlet Mach number of 1.7

Figs. 18 and 19 show a comparison of Mach number contours and wave structures for a single strut and a strut cavity combustor, respectively, when the main flow enters the isolator at Ma=1.7. Compared with the results of the single strut combustor, the pre-combustion shock waves in the strut-cavity combustor are closer to the entrance. As a result, the pre-combustion shock waves are not pushed out of isolator until the wall-injection pressure increases to 4.0 atm. This means that the combustor with cavities can work with a higher wall-injection pressure, but at a price of a lower Mach number behind the strut, because of much larger subsonic zones.

Figs. 20 and 21 (p.446) allow a comparison of the combustion performance of the two combustors at different wall-injection pressures when the main flow enters at Ma=1.7. When the cavities are present, the mixing efficiency decreases slightly, and the case without wall-injection is affected (compare Fig. 20a with Fig. 21a). The combustion efficiency also declines when using the strut-cavity combustor (compare Fig. 20b with Fig. 21b). The average Mach number obtained by the strut-cavity combustor is slightly lower than that obtained by the single strut combustor (compare Fig. 20c with Fig. 21c). The strut-cavity combustor has an advantage over the single strut combustor in terms of total pressure recovery (compare Fig. 21d with Fig. 22d (p.446)). This

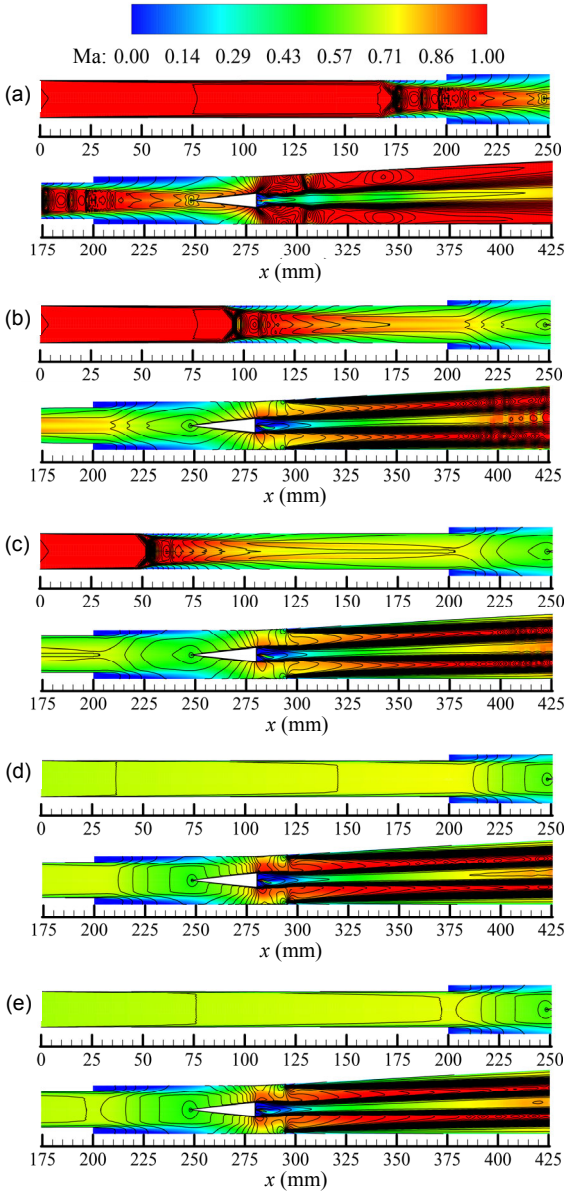

Fig. 18 Mach number contours and wave structures obtained by a single strut combustor at different wall-injection pressures: (a) $P_{j\text{-}w}$=0; (b) $P_{j\text{-}w}$=2.5 atm; (c) $P_{j\text{-}w}$=3.0 atm; (d) $P_{j\text{-}w}$=3.5 atm; (e) $P_{j\text{-}w}$=4.0 atm

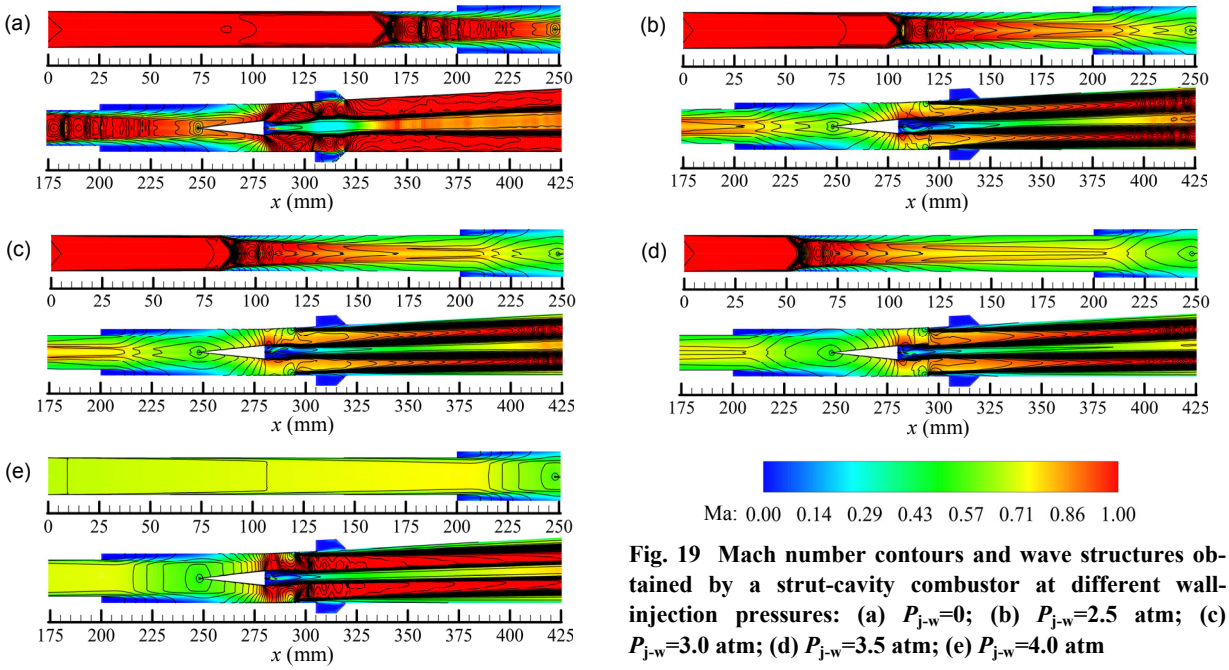

Fig. 19 Mach number contours and wave structures obtained by a strut-cavity combustor at different wall-injection pressures: (a) $P_{j\text{-}w}$=0; (b) $P_{j\text{-}w}$=2.5 atm; (c) $P_{j\text{-}w}$=3.0 atm; (d) $P_{j\text{-}w}$=3.5 atm; (e) $P_{j\text{-}w}$=4.0 atm

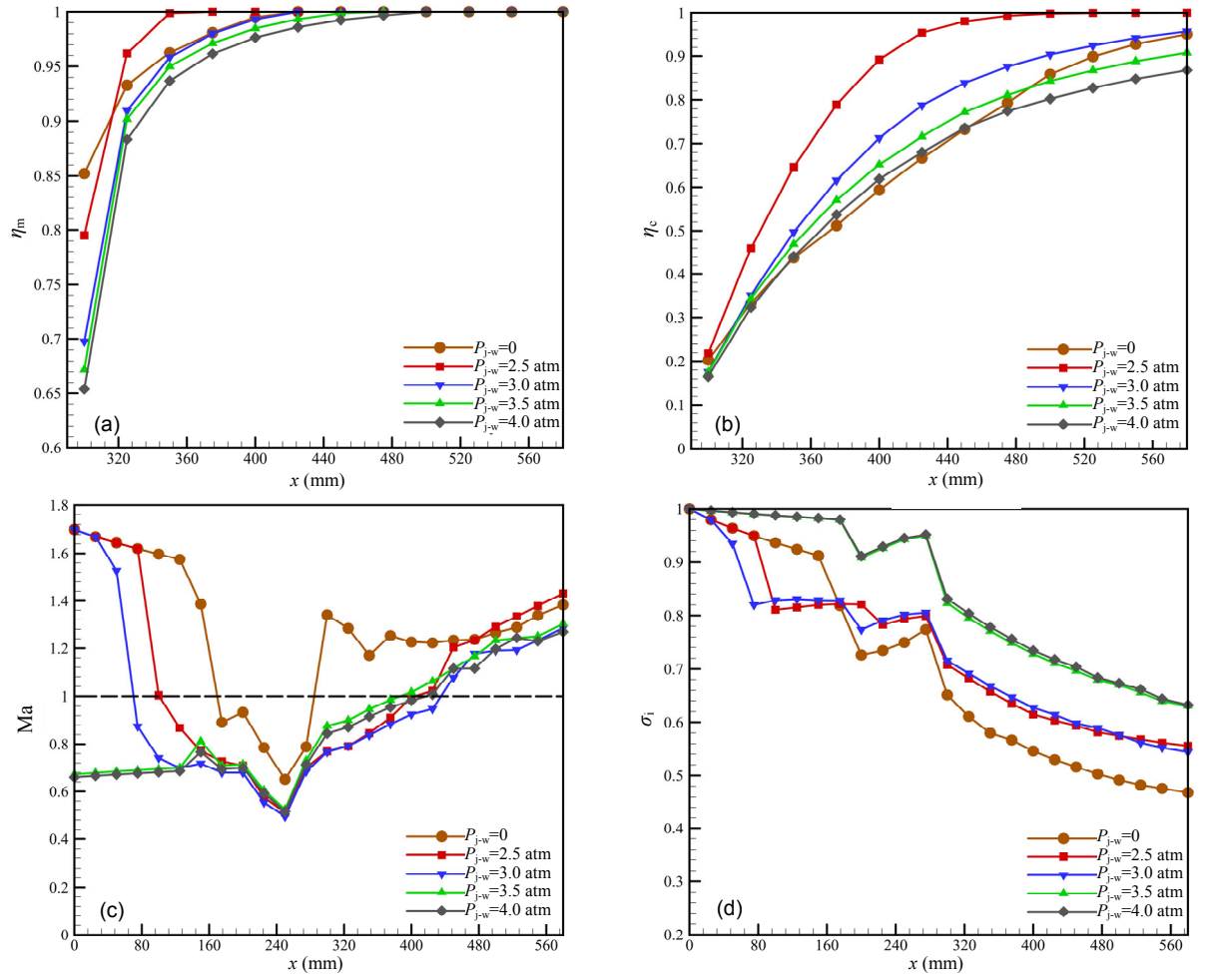

Fig. 20 Comparison of combustion performance using a single strut combustor at different wall-injection pressures
(a) Mixing efficiency; (b) Combustion efficiency; (c) Mass-weighted Mach number; (d) Total pressure recovery

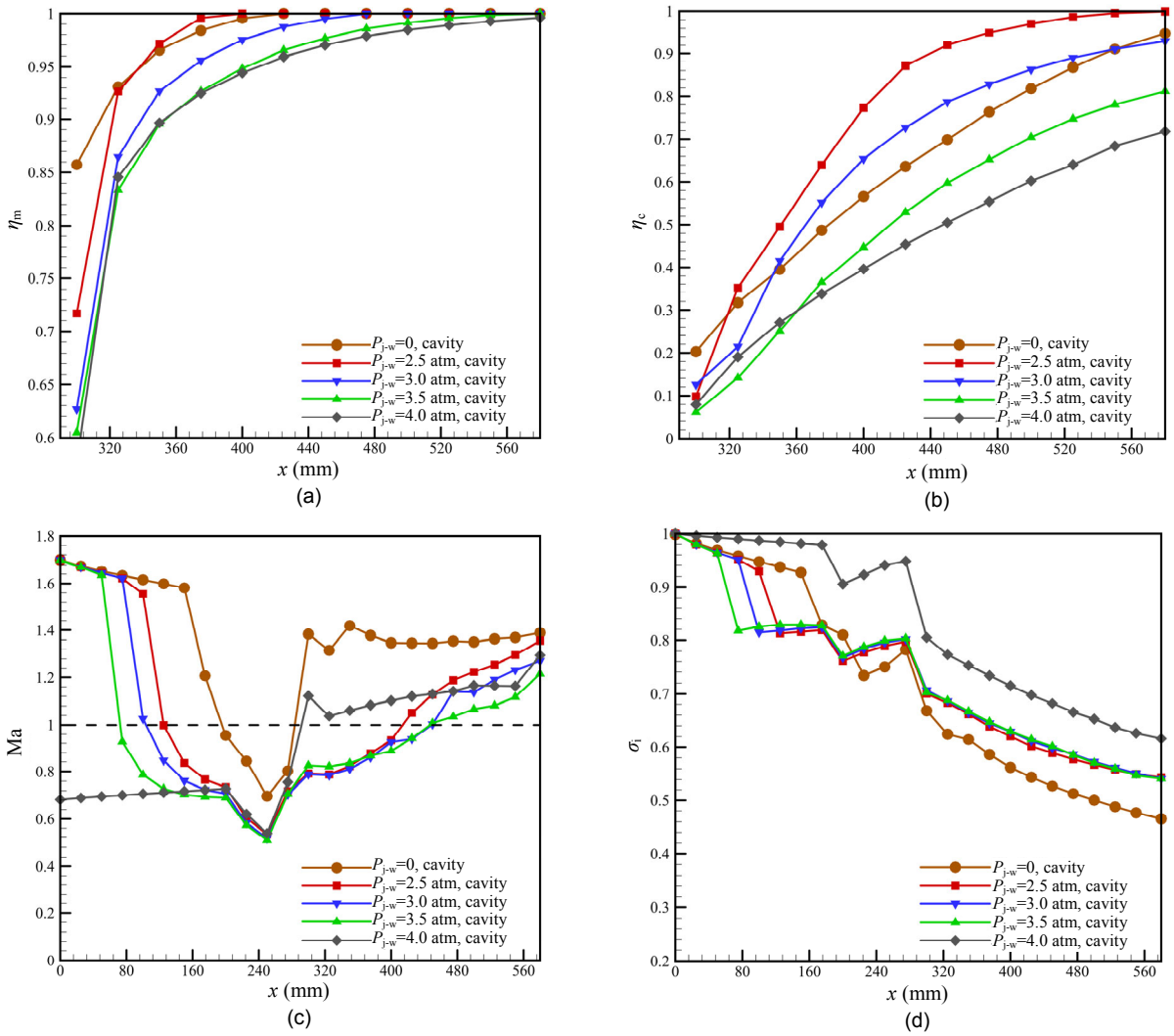

Fig. 21 Comparison of combustion performance using a strut-cavity combustor at different wall-injection pressures
(a) Mixing efficiency; (b) Combustion efficiency; (c) Mass-weighted Mach number; (d) Total pressure recovery

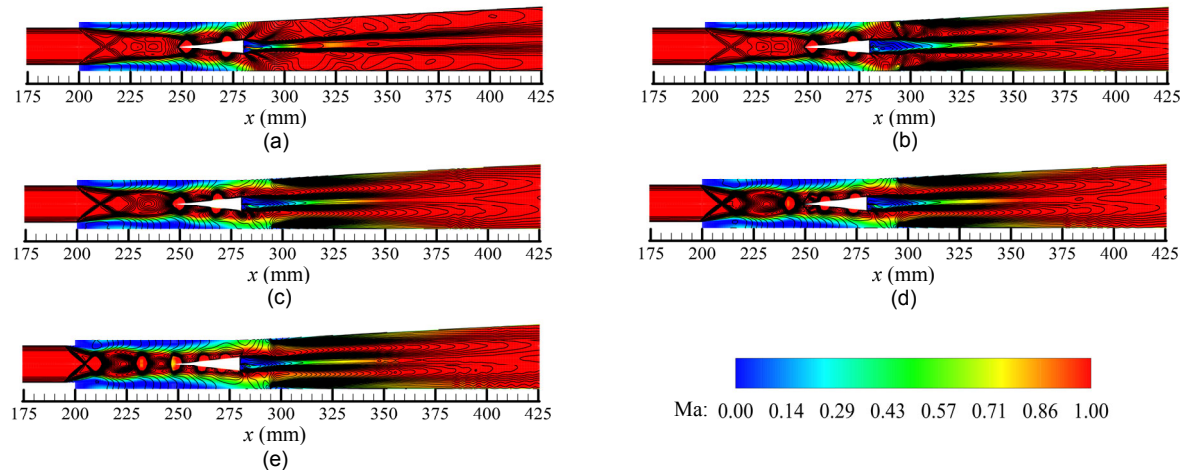

Fig. 22 Mach number contours and wave structures obtained by a single strut combustor for different wall-injection pressures: (a) $P_{j\text{-}w}$=0; (b) $P_{j\text{-}w}$=6.0 atm; (c) $P_{j\text{-}w}$=7.5 atm; (d) $P_{j\text{-}w}$=9.0 atm; (e) $P_{j\text{-}w}$=10.99 atm

result may be a little unexpected. Generally, the cavity would improve the mixing and combustion efficiency because it enlarges the low-velocity zone. However, the length of the cavity may be too small to allow the formation of a recirculation zone near the cavity (Mahto et al., 2016). However, this kind of cavity can reduce the interaction between pre-combustion shock waves and the intense pressure rise caused by combustion, thereby helping to stabilize the combustion.

4.2.2 Inlet Mach number of 2.1

Figs. 22 and 23 allow a comparison of the Mach number contours of the two combustors when the main flow enters the isolator at Ma=2.1. Ma=2.1 might be the transition point for this combustor, so this is a meaningful comparison. When employing the strut-cavity combustor, the separation zones generated on both the upper and lower walls are smaller than when a single strut combustor is used, especially when the wall-injection pressure is lower. The shock waves in front of the strut are also much weaker. At this point, the use of cavities may precipitate the transition from ramjet to scramjet, because a significant phenomenon of the scramjet mode is the disappearance of pre-combustion shock waves. Behind the strut, the cavities cause a more intense interaction between the reflected shock wave and the mixing layer, thereby creating larger subsonic regions.

Figs. 24 and 25 (p.449) allow a comparison of combustion performance at different wall-injection pressures for the two combustors, when the main flow enters at Ma=2.1. The results here are similar to those at Ma=1.7. Compared with the single strut combustor, the strut-cavity combustor has a lower mixing and combustion efficiency, lower average Mach number, and better total pressure recovery. Note that in Fig. 24d, the total pressure recovery of the case without wall-injection is lower than that of the others, but in Fig. 25d, the results are opposite. This situation is similar to the case using a single strut combustor at Ma=2.3 (Fig. 16d).

5 Conclusions

In this study, the influence of wall-injection pressure on a typical strut-based dual-mode scramjet combustor was investigated numerically, and the effect of typical cavities evaluated qualitatively. By comparing the Mach number contours and wave structures, mixing and combustion efficiency, 1D mass-weighted average Mach number, and total pressure recovery, we have come to the following conclusions:

1. The wall-injection pressure has a great influence on the flow field structures, especially the ram-to-scram mode transition and the combustion performance. A high wall-injection pressure will cause some problems: in the ramjet mode, it might push the pre-combustion shock waves out of the

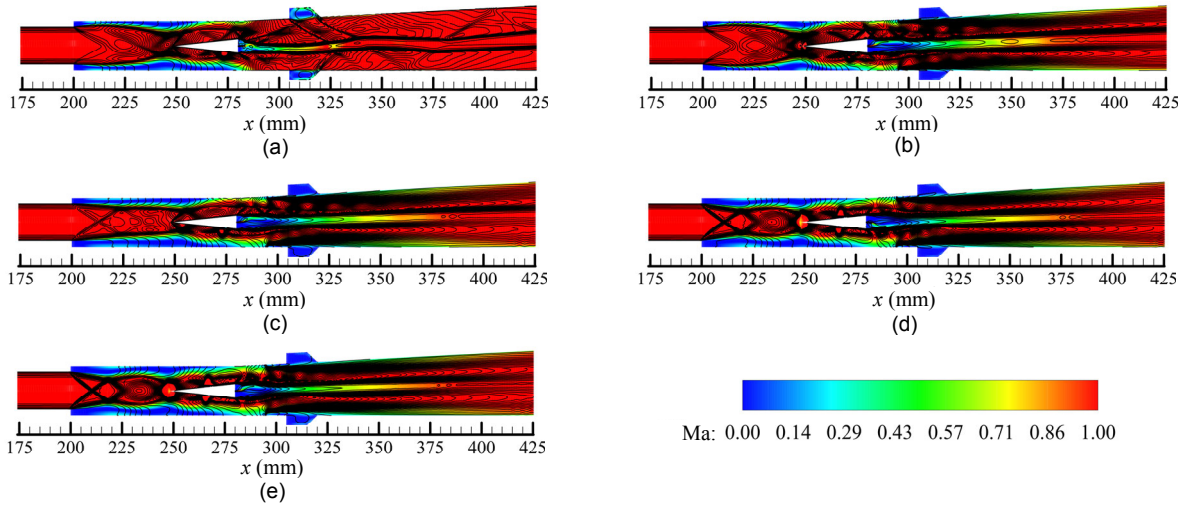

Fig. 23 Mach number contours and wave structures obtained by a strut-cavity combustor at different wall-injection pressures: (a) $P_{j\text{-}w}$=0; (b) $P_{j\text{-}w}$=6.0 atm; (c) $P_{j\text{-}w}$=7.5 atm; (d) $P_{j\text{-}w}$=9.0 atm; (e) $P_{j\text{-}w}$=10.99 atm

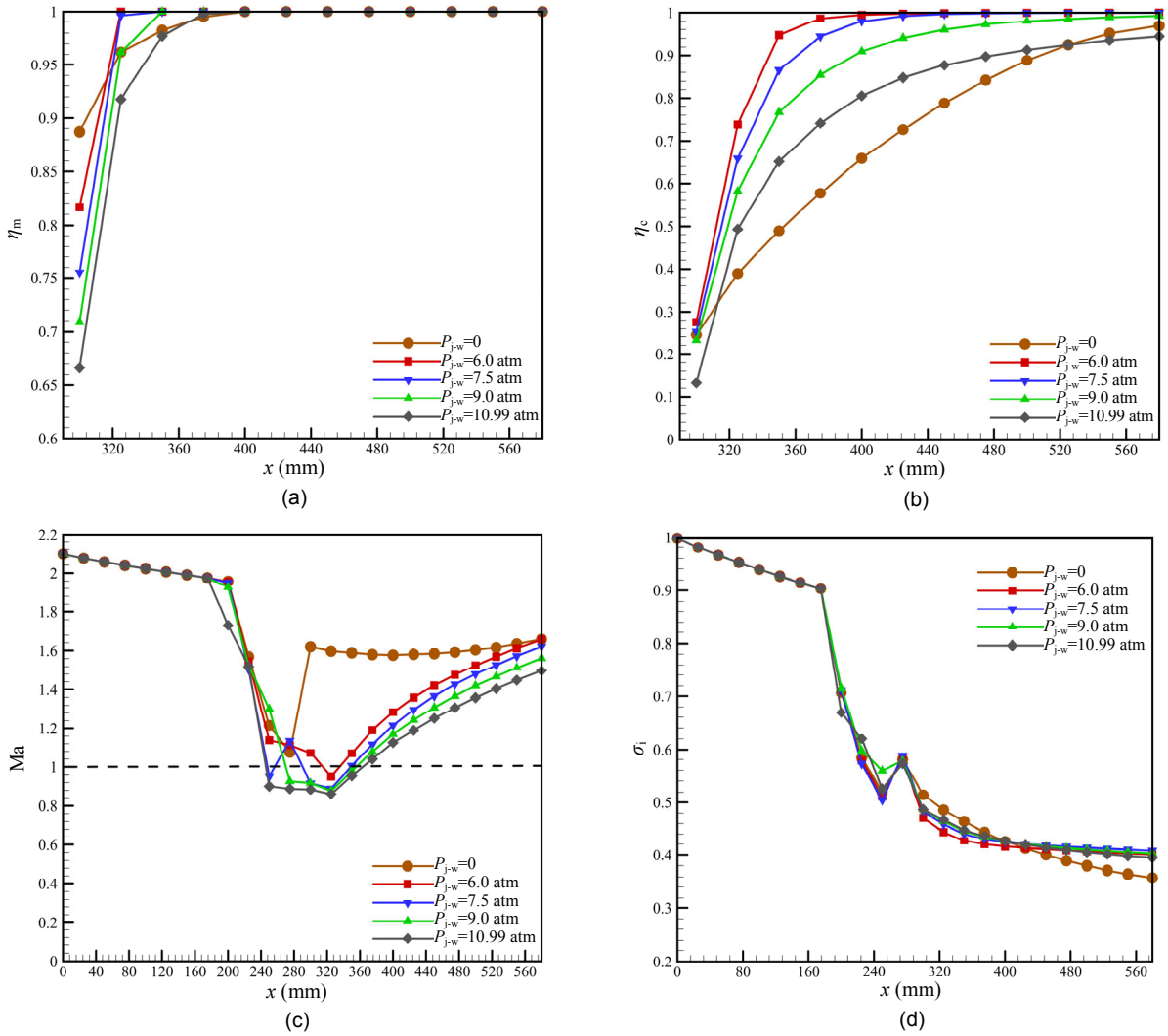

Fig. 24 Comparison of combustion performance using a single strut combustor at different wall-injection pressures at Ma=2.1
(a) Mixing efficiency; (b) Combustion efficiency; (c) Mass-weighted Mach number; (d) Total pressure recovery

isolator, while in scramjet mode, the combustor is likely to suffer huge energy loss because of the high wall-injection pressure. For all the cases studied, a wall-injection pressure of about half of the strut-injection pressure seems to be the best.

2. The cavity adopted in this study would prevent the pre-combustion shock waves from pushing out of the isolator and help to stabilize the flow field, but it would decrease the mixing and combustion efficiency. Clearly, there is a great scope for further investigation of the optimization of the strut-cavity combination. At the same time, a cavity has been shown to reduce the transition time from the scram mode to the ram mode, implying that a combustor with a cavity is beneficial for the scram mode.

References

Cao RF, Chang JT, Tang JF, et al., 2014. Study on combustion mode transition of hydrogen fueled dual-mode scramjet engine based on thermodynamic cycle analysis. *International Journal of Hydrogen Energy*, 39(36):21251-21258. https://doi.org/10.1016/j.ijhydene.2014.10.082

Choubey G, Pandey KM, 2016. Investigation on the effects of operating variables on the performance of two-strut scramjet combustor. *International Journal of Hydrogen Energy*, 41(45):20753-20770. https://doi.org/10.1016/j.ijhydene.2016.09.157

Choudhuri AR, Gollahalli SR, 2000. Combustion characteristics of hydrogen-hydrocarbon hybrid fuels. *International Journal of Hydrogen Energy*, 25(5):451-462. https://doi.org/10.1016/S0360-3199(99)00027-0

Curran ET, 2001. Scramjet engines: the first forty years. *Journal of Propulsion and Power*, 17(6):1138-1148.

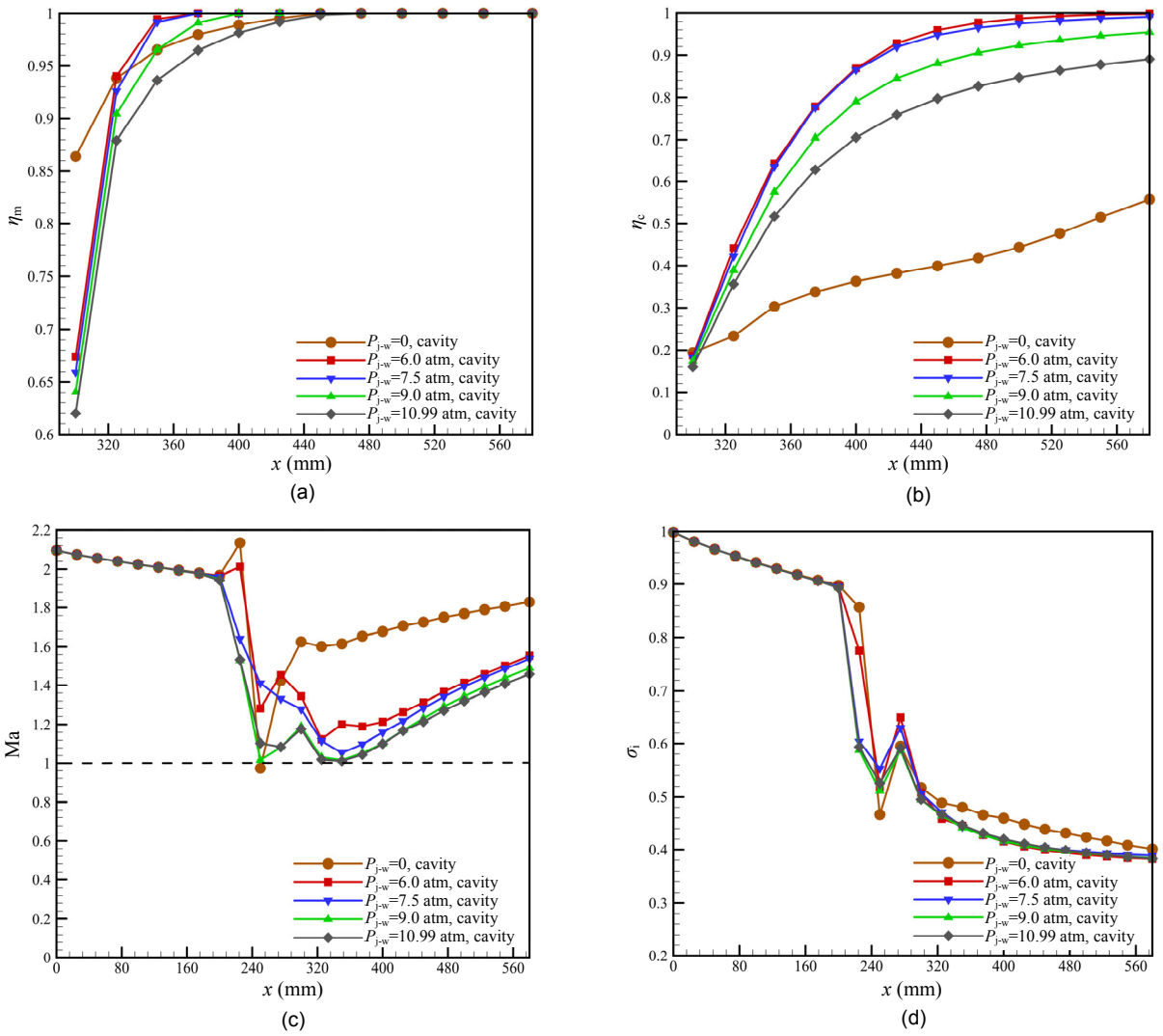

Fig. 25 Comparison of combustion performance using a strut-cavity combustor at different wall-injection pressures at Ma=2.1
(a) Mixing efficiency; (b) Combustion efficiency; (c) Mass-weighted Mach number; (d) Total pressure recovery

https://doi.org/10.2514/2.5875

Fluent, 2006. Fluent 6.3 User's Guide. Fluent, Inc., Lebanon, USA.

Fureby C, Nordin-Bates K, Petterson K, et al., 2015. A computational study of supersonic combustion in strut injector and hypermixer flow fields. *Proceedings of the Combustion Institute*, 35(2):2127-2135. https://doi.org/10.1016/j.proci.2014.06.113

Gang Q, Zhou LY, Qin Z, et al., 2011. Experimental investigation of strut-cavity flameholder technology in liquid hydrocarbon fueled scramjet combustor. *Journal of Propulsion Technology*, 32:680-683 (in Chinese).

Gruber MR, 2004. Mixing and combustion studies using cavity-based flameholders in a supersonic flow. *Journal of Propulsion and Power*, 20(5):769-778. https://doi.org/10.2514/1.5360

Guerra R, Waidmann W, Laible C, 1991. An experimental investigation of the combustion of a hydrogen jet injected parallel in a supersonic air stream. AIAA 3rd International Aerospace Planes Conference, AIAA Paper 91-5102.

Huang W, 2015. Investigation on the effect of strut configurations and locations on the combustion performance of a typical scramjet combustor. *Journal of Mechanical Science and Technology*, 29(12):5485-5496. https://doi.org/10.1007/s12206-015-1150-6

Huang W, 2016. Transverse jet in supersonic crossflows. *Aerospace Science and Technology*, 50:183-195. https://doi.org/10.1016/j.ast.2016.01.001

Huang W, Yan L, 2013. Progress in research on mixing techniques for transverse injection flow fields in supersonic crossflows. *Journal of Zhejiang University-SCIENCE A*

(Applied Physics & Engineering), 14(8):554-564. https://doi.org/10.1631/jzus.A1300096

Huang W, Yan L, 2016. Numerical investigation on the ram-scram transition mechanism in a strut-based dual-mode scramjet combustor. *International Journal of Hydrogen Energy*, 41(8):4799-4807. https://doi.org/10.1016/j.ijhydene.2016.01.062

Huang W, Wang ZG, Jin L, et al., 2011a. Effect of cavity location on combustion flow field of integrated hypersonic vehicle in near space. *Journal of Visualization*, 14(4):339-351. https://doi.org/10.1007/s12650-011-0100-3

Huang W, Wang ZG, Pourkashanian M, et al., 2011b. Numerical investigation on the shock wave transition in a three-dimensional scramjet isolator. *Acta Astronautica*, 68(11-12):1669-1675. https://doi.org/10.1016/j.actaastro.2010.12.011

Huang W, Wang ZG, Luo SB, et al., 2011c. Parametric effects on the combustion flow field of a typical strut-based scramjet combustor. *Chinese Science Bulletin*, 56(35): 3871-3877. https://doi.org/10.1007/s11434-011-4823-2

Huang W, Pourkashanian M, Ma L, et al., 2012a. Effect of geometric parameters on the drag of the cavity fame-holder based on the variance analysis method. *Aerospace Science and Technology*, 21(1):24-30. https://doi.org/10.1016/j.ast.2011.04.009

Huang W, Ma L, Pourkashanian M, et al., 2012b. Flow-field analysis of a typical hydrogen-fueled dual-mode scramjet combustor. *Journal of Aerospace Engineering*, 25(3): 336-346. https://doi.org/10.1061/(ASCE)AS.1943-5525.0000136

Huang W, Liu WD, Li SB, et al., 2012c. Influences of the turbulence model and the slot width on the transverse slot injection flow field in supersonic flows. *Acta Astronautica*, 73:1-9. https://doi.org/10.1016/j.actaastro.2011.12.003

Huang W, Wang ZG, Yan L, et al., 2012d. Numerical validation and parametric investigation on the cold flow field of a typical cavity-based scramjet combustor. *Acta Astronautica*, 80:132-140. https://doi.org/10.1016/j.actaastro.2012.06.004

Huang W, Li SB, Yan L, et al., 2013. Performance evaluation and parametric analysis on cantilevered ramp injector in supersonic flows. *Acta Astronautica*, 84:141-152. https://doi.org/10.1016/j.actaastro.2012.11.011

Huang W, Jin L, Yan L, et al., 2014a. Influence of jet-to-crossflow pressure ratio on nonreacting and reacting processes in a scramjet combustor with backward-facing steps. *International Journal of Hydrogen Energy*, 39: 21242-21250. https://doi.org/10.1016/j.ijhydene.2014.10.073

Huang W, Yan L, Tan JG, 2014b. Survey on the mode transition technique in combined cycle propulsion systems. *Aerospace Science and Technology*, 39:685-691. https://doi.org/10.1016/j.ast.2014.07.006

Huang W, Li SB, Yan L, et al., 2015. Multiobjective design optimization of a cantilevered ramp injector using the surrogate-assisted evolutionary algorithm. *Journal of Aerospace Engineering*, 28:04014138. https://doi.org/10.1061/(ASCE)AS.1943-5525.0000477

Huang W, Li MH, Yan L, 2016a. Mixing augmentation mechanism induced by the pseudo shock wave in transverse gaseous injection flow fields. *International Journal of Hydrogen Energy*, 41:10961-10968. https://doi.org/10.1016/j.ijhydene.2016.04.078

Huang W, Li LQ, Yan L, et al., 2016b. Numerical exploration of mixing and combustion in a dual-mode combustor with backward-facing steps. *Acta Astronautica*, 127:572-578. https://doi.org/10.1016/j.actaastro.2016.06.043

Huang W, Li MH, Ding F, 2016c. Supersonic mixing augmentation mechanism induced by a wall-mounted cavity configuration. *Journal of Zhejiang University-SCIENCE A (Applied Physics & Engineering)*, 17(1):45-53. https://doi.org/10.1631/jzus.A1500244

Kim CH, Jeung IS, Choi B, et al., 2011. Effect of fuel injection location on a plasma jet assisted combustion with a backward-facing step. *Proceedings of the Combustion Institute*, 33:2375-2382. https://doi.org/10.1016/j.proci.2010.07.057

Kummitha OR, Pandey KM, Gupta R, 2018. CFD analysis of a scramjet combustor with cavity based flame holders. *Acta Astronautica*, 144:244-253. https://doi.org/10.1016/j.actaastro.2018.01.005

Mahto NK, Choubey G, Suneetha L, et al., 2016. Effect of variation of length-to-depth ratio and Mach number on the performance of a typical double cavity scramjet combustor. *Acta Astronautica*, 128:540-550. https://doi.org/10.1016/j.actaastro.2016.08.010

Micka DJ, Driscoll JF, 2009. Combustion characteristics of a dual-mode scramjet combustor with cavity flameholder. *Proceedings of the Combustion Institute*, 32(2):2397-2404. https://doi.org/10.1016/j.proci.2008.06.192

Oevermann M, 2000. Numerical investigation of turbulent hydrogen combustion in a SCRAMJET using flamelet modeling. *Aerospace Science Technology*, 4(7):463-480. https://doi.org/10.1016/S1270-9638(00)01070-1

Ogawa H, 2016. Effects of injection angle and pressure on mixing performance of fuel injection via various geometries for upstream-fuel-injected scramjets. *Acta Astronautica*, 128:485-498. https://doi.org/10.1016/j.actaastro.2016.08.008

Qin J, Bao W, Zhou WX, et al., 2010. Flow and heat transfer characteristics in fuel cooling channels of a recooling cycle. *International Journal of Hydrogen Energy*, 35(19): 10589-10598. https://doi.org/10.1016/j.ijhydene.2010.08.019

Segal C, 2009. The Scramjet Engine Processes and Characteristics. Cambridge University Press, UK.

Smirnov NN, Nikitin VF, 2014. Modeling and simulation of hydrogen combustion in engines. *International Journal of Hydrogen Energy*, 39(2):1122-1136. https://doi.org/10.1016/j.ijhydene.2013.10.097

Smirnov NN, Nikitin VF, Phylippov YG, 2010. Deflagration to detonation transition in gases in tubes with cavities. *Journal of Engineering Physics and Thermophysics*, 83(6):1287-1316. https://doi.org/10.1007/s10891-010-0448-6

Smirnov NN, Betelin VB, Nikitin VF, et al., 2015. Accumulation of errors in numerical simulations of chemically reacting gas dynamics. *Acta Astronautica*, 117:338-355. https://doi.org/10.1016/j.actaastro.2015.08.013

Tian Y, Xiao BG, Zhang SP, et al., 2015. Experimental and computational study on combustion performance of a kerosene fueled dual-mode scramjet engine. *Aerospace Science and Technology*, 46:451-458. https://doi.org/10.1016/j.ast.2015.09.002

Turner JC, Smart MK, 2010. Application of inlet injection to a three-dimensional scramjet at Mach 8. *AIAA Journal*, 48(4):829-838. https://doi.org/10.2514/1.J050052

Yan L, Liao L, Huang W, et al., 2018. Nonlinear process in the mode transition in typical strut-based and cavity-strut based scramjet combustors. *Acta Astronautica*, 145:250-262. https://doi.org/10.1016/j.actaastro.2018.01.061

Zhang Y, Zhu SH, Chen B, et al., 2016. Hysteresis of mode transition in a dual-struts based scramjet. *Acta Astronautica*, 128:147-159. https://doi.org/10.1016/j.actaastro.2016.07.025

中文概要

题　目：基于支板的超燃冲压发动机燃烧室模态转换过程参数化研究

目　的：超燃冲压发动机燃烧室中氢气的燃烧性能引起了研究者的广泛兴趣。本文旨在探讨不同压比下超燃冲压发动机燃烧室的燃烧性能以及壁面凹腔的影响，为双模态超燃冲压发动机燃烧室设计提供参考。

创新点：1. 研究压比变化过程中超燃向亚燃的转换过程；2. 研究壁面凹腔设置对模态转换过程的影响。

方　法：采用数值模拟方法研究不同来流条件下，压比和壁面凹腔设置对基于支板的超燃冲压发动机燃烧室中模态转换过程的影响。

结　论：1. 壁面喷注压强对流场结构影响很大，特别是对于亚燃到超燃的模态转换过程和燃烧性能，当壁面喷注压强大约为支板喷注压强一半时，效果最好；2. 壁面凹腔能帮助稳定流场，但也会带来一定的混合效率和燃烧效率损失，同时壁面凹腔能帮助延迟从超燃模态向亚燃模态的转换时间，这也从一定程度上说明带凹腔的燃烧室更加适合于超燃模态。

关键词：超燃冲压发动机；模态转换；支板；凹腔；燃烧性能